AIMS Materials Science, 12(6): 1215–1240.
DOI: 10.3934/matersci.2025056
Received: 12 June 2025
Revised: 20 November 2025
Accepted: 01 December 2025
Published: 05 December 2025

https://www.aimspress.com/journal/Materials

Research article

Influence of gas mixture on the mechanical and physical properties of CrN coatings obtained by magnetron sputtering method

Bauyrzhan Rakhadilov[1], Nazerke Muktanova[1,*], Dastan Buitkenov[2], Yernar Turabekov[1,3], Elvira Akhmetova[1,3] and Merkhat Dautbekov[1]

[1] PlasmaScience LLP, Ust-Kamenogorsk 070018, Kazakhstan
[2] Research Center "Surface Engineering and Tribology", Sarsen Amanzholov East Kazakhstan University, Ust-Kamenogorsk 070000, Kazakhstan
[3] Daulet Serikbaev East Kazakhstan Technical University, Ust-Kamenogorsk 070002, Kazakhstan

* **Correspondence:** Email: muktanovan@gmail.com; Tel: +7-747-730-0937.

Abstract: This paper investigated the influence of the Ar/N_2 working gas mixture composition on the morphological, structural, mechanical, and corrosion properties of single-layer CrN coatings obtained by reactive magnetron sputtering on E110 zirconium alloy substrates. It was shown that an increase in the N_2 fraction in the working gas leads to a sequential compaction of the coating structure, an increase in the degree of nitride formation, and the formation of a more homogeneous cubic CrN phase (Fm-3m), which was confirmed by Grazing-Incidence X-Ray Diffraction data (GI-XRD). Scanning electron microscopy (SEM) analysis revealed a transition from a relatively loose morphology at 90/30 sccm to a denser and finer-grained structure at 80/40 sccm. It was established that an increase in the partial pressure of nitrogen contributes to a decrease in surface roughness (Ra from 0.152 to 0.114 μm) and an increase in nanohardness from 4.1 to 6.7 GPa, as well as Young's modulus from 97 to 110 GPa, associated with the formation of a denser and closer to stoichiometric CrN phase. Electrochemical tests in 3.5% NaCl showed a significant improvement in corrosion resistance; the corrosion current density decreased from 3.82×10^{-6} to 1.73×10^{-6} A/cm^2, and the corrosion rate decreased from 0.054 to 0.0024 mm/year.

Keywords: CrN; magnetron sputtering; zirconium alloys; hardness; phase composition; mechanical properties; coatings

1. Introduction

Zirconium alloys (in particular, Zr-4) are widely used as materials for fuel element cladding in light water nuclear reactors (LWRs) due to their high thermal conductivity, low thermal neutron capture cross section, high mechanical strength, and excellent corrosion resistance [1–5]. However, in loss-of-coolant accidents (LOCA), they undergo an intense reaction with water vapor, accompanied by significant hydrogen and heat release, which can lead to serious consequences, as was recorded in the accident at the Fukushima nuclear power plant in 2011 [6,7]. In this regard, the concept of accident-tolerant fuel (ATF) was proposed, aimed at improving the operational reliability and stability of fuel cladding under extreme conditions. One of the most practical and effective approaches to implementing ATF is to apply a protective coating to the surface of Zr-4 alloys. This method avoids the need to modify existing production equipment and thus facilitates its industrial implementation in the short term [8–10].

Current research into candidate coatings for ATF focuses on ceramic (Ti_2AlC, TiN, AlCrN, CrN) [11–13] and metal coatings (FeCrAl, Mo, Cr) [14,15]. All of them demonstrate the ability to significantly increase the oxidation and corrosion resistance of zirconium alloys. Chromium-based coatings are considered particularly promising due to their high resistance to oxidation [16–18]. However, Cr oxidation is accompanied by the formation of a Cr_2O_3 oxide film with a Peeling–Bedworth coefficient of 2.07 [19], which leads to the development of internal stresses and, as a result, to cracking and delamination of the coating [20]. In addition to the barrier functions of the coating, it is necessary to consider the compatibility of the mechanical properties and thermal expansion coefficients between the coating and the substrate. In this context, nitride coatings (TiN, ZrN, CrN) are of particular interest because they are characterized by high hardness, wear resistance, thermal stability, and corrosion resistance [21–25]. Among them, CrN stands out as one of the most promising candidates due to its balanced combination of physical, mechanical, and chemical characteristics [26–29].

In a number of studies, such as the work by Adesinaet al. [30], comparative analysis of coatings obtained by cathodic arc physical vapor deposition (PVD) (including TiN, CrN, AlTiN, and AlCrN) showed that CrN has the lowest friction coefficient and the highest adhesion strength. In the work of Ali et al. [31], the corrosion and surface properties of TiN, ZrN, and CrN coatings applied to β-titanium alloys by PVD were investigated. It was found that CrN demonstrates high corrosion resistance and reliable adhesion. TiN-, CrN-, and TiB_2-based materials have high melting points, high hardness, good mechanical properties, and thermal stability, which makes them promising for use in aggressive environments. According to the literature [32], CrN coatings show higher operational efficiency compared to TiN and ZrN, making them the preferred choice for functional coatings.

CrN can be obtained by various methods of PVD, including magnetron sputtering, arc evaporation, ion-plasma spraying, and electron beam evaporation [33–36]. In recent decades, magnetron sputtering has been rapidly developing as one of the most versatile and widely used PVD methods [37–40]. This method allows obtaining dense, homogeneous, and precisely controlled coatings in terms of thickness, which in some cases demonstrate functionality comparable to thicker coatings obtained by alternative methods [41–44]. In addition, this method makes it possible to vary the technological parameters of deposition (e.g., substrate temperature, pressure, power, gas flow rate and composition, and process duration), which allows for flexible control of the structure and properties of the coatings obtained [45–48].

Variation of the technological parameters of the reactive magnetron sputtering method allows obtaining CrN coatings of different phase composition and morphology, which causes significant differences in their properties. Thus, Kong et al. [49] investigated the effect of nitrogen content (20%–60%) in the Ar/N_2 gas mixture during film deposition on 1Cr18Mn8Ni5N steel substrates. It was found that the atomic concentration of nitrogen in the coating increases with an increase in the N_2 fraction, with a pure CrN phase forming at 50%. All coatings had a typical columnar morphology (T zone according to Thornton's model). The mixed phases Cr_2N and Cr(N) were characterized by low hardness and high friction coefficient, while Cr_2N exhibited higher hardness and CrN exhibited a lower friction coefficient. Zhang et al. [50] showed that the deposition rate of CrN coatings decreases with increasing nitrogen content in the Ar/N_2 mixture. The phase composition included Cr, Cr_2N, and CrN, and the crystallographic texture varied significantly depending on the conditions. Dense coatings were formed at low N_2 flow rates. Hardness and plasticity did not show a direct dependence on gas composition. Ahmad et al. [51] used pulsed magnetron sputtering in an Ar–N_2 atmosphere on AISI-304 substrates to study the effect of discharge power (100–200 W) and N_2 concentration (5%–20%). X-ray structural analysis showed the formation of CrN phases with varying degrees of crystallinity. Maximum hardness and coating thickness (~755 nm) were achieved at a power of 150 W and a nitrogen content of 5%. Zhang et al. [52] found that an increase in the N_2 content leads to a decrease in the deposition rate and a change in the surface morphology, from loose pyramidal to dense spherical. At low nitrogen content, Cr_2N and Cr phases prevailed, while at high concentrations, single-phase CrN was formed. The orientation of the crystallites shifted to (111). Maximum adhesion was observed at N_2/Ar = 30:40, although the bond strength tended to decrease. Zhang et al. [53] showed that when the N_2 concentration was varied from 0% to 60%, the phase composition of the coatings changed from bcc-Cr to Cr_2N + Cr, then to an amorphous structure, and with further nitrogen growth, to stable CrN. The morphology was columnar (Thornton's T/I transition zone). Subramanian et al. [54] deposited CrN films by DC sputtering on glass and silicon substrates. Analysis showed the presence of Cr_2N and CrN phases. The average grain size increased with increasing nitrogen supply, and the morphology had a dense columnar structure. Electrophysical measurements revealed semiconductor behavior at a flow rate of N_2 = 15 sccm. Shah et al. [55] demonstrated the influence of gas atmosphere composition (Ar or He) and substrate temperature on the properties of CrN coatings obtained on SA-304 steel. It was found that with an increase in N_2 content, the average grain size decreases and the structure becomes denser. In the He + N_2 atmosphere, films were thinner and had smaller grains than in Ar + N_2. At a nitrogen content of up to 30%, a CrN + Cr_2N phase was formed, which had higher microhardness (16.95 GPa) than single-phase CrN (10.5 GPa). He et al. [56] showed that an increase in the N_2 content in the Ar/N_2 mixture reduces the film thickness (1.5 to 1.3 μm), causes a shift in the preferred orientation from (200) to (111), and also changes the nature of the residual stresses (from compressive to tensile). CrN films with $x < 1$ had increased hardness due to grain refinement and anionic vacancies. During thermal testing (500–650 °C), the coatings retained high hardness, but at 800 °C, degradation occurred due to oxidation and oxygen diffusion.

Based on the results of the literature review, a correlation table (Table 1) was created, which is presented below.

Table 1. Effect of N_2 content on the phase composition and properties of CrN coatings.

Literature	Gas composition/mode	Substrate/method	Phases	Morphology/density	Key properties
Kong et al., 2011 [49]	Ar/N_2 = 20%–60%; at 50% N_2→pure CrN	1Cr18Mn8Ni5N; medium-frequency magnetron sputtering	Cr, Cr_2N, CrN; at 50% N_2, CrN phase; T zone (Thornton)	Columnar	At 50% N_2, CrN is formed; Cr_2N→↑hardness, CrN→↓friction coefficient
Zhang et al., 2014 [50]	Ar/N_2: N_2 (99.9%): 9, 12, 15, 18, 21 SCCM Ar (99.9%): 21, 18, 15, 12, 9 SCCM	Stainless steel 1Cr18Ni9Ti; magnetron sputtering	Cr, Cr_2N, CrN; texture depends on N_2	Dense at low N_2	Deposition rate ↓ with increasing N_2; hardness and adhesion: no direct dependence on N_2
Ahmad et al., 2013 [51]	Ar 95% + N_2 5%–20%; power 100–200 W; maximum at 150 W, 5% N_2	AISI-304; pulsed DC magnetron sputtering	CrN	Grainy surface	Thickness ≈ 755 nm and max. hardness at 150 W and 5% N_2
Zhang et al., 2016 [52]	N_2 variation; N_2/Ar = 30:40→max. adhesion	304 stainless steel; single-target magnetron sputtering	At low N_2: Cr_2N + Cr; at high N_2: predominantly CrN	Pyramidal (low N_2)→spherical (high N_2)	With increasing N_2: Precipitation rate ↓, density ↑, hardness ↑
Zhang et al., 2007 [53]	0% N_2	Silicon Si; medium-frequency magnetron sputtering	bcc-Cr	Columnar (T/I zone)	Lower COF (coefficient of friction) with steel counterbody (comparative trend)
	20% N_2		Mixed phase Cr_2N + Cr	Columnar (T/I zone)	COF decreases; minimum in the range of 20%–40% N_2
	40% N_2		Amorphous structure	Transitional columnar	Minimum COF is maintained (20%–40% N_2)
	≥60% N_2		Stable CrN	Columnar (T/I zone)	COF stabilizes (~0.7, as a general trend)
Subramanian et al., 2012 [54]	N_2 flow varies; N_2 = 15 sccm → semiconductor behavior	Glass, Si; medium-frequency magnetron sputtering	Cr_2N + CrN	Dense columnar; grain size ↑ with increasing N_2	EDS: uniform composition; semiconductor at 15 sccm

Continued on next page

Literature	Gas composition/mode	Substrate/method	Phases	Morphology/density	Key properties
Shah et al., 2010 [55]	Ar + N_2 or He + N_2; increase in substrate temperature and N_2	SA-304 steel; DC reactive magnetron sputtering	CrN + Cr_2N up to 30% N_2; CrN appears at high nitrogen content	Denser at ↑ temperature and ↑ N_2; He + N_2→thin, fine grained	Coatings with CrN + Cr_2N phase demonstrate high hardness of 16.95 GPa; CrN: 10.50 GPa
He et al., 2021 [56]	Increase in N_2 content	Silicon Si; magnetron sputtering	CrN_x	Dense	Film thickness decreased from 1.5 to 1.3 μm with an increase in N_2 flow rate; hardness ↑; thermal stability up to 500–650 °C; degradation ≥800 °C

As shown by a review of the literature, the structure and properties of CrN coatings obtained by PVD methods depend on many factors, such as substrate temperature, pressure, power, gas flow rate and composition, and process duration. In addition to these factors, the design of the installation itself also has a significant impact. Furthermore, experiments often contradict each other due to differences in the conditions under which they are conducted, making it necessary to accumulate a large database in order to identify true patterns and establish reliable scientific conclusions for the practical use of CrN-based coatings in reactor construction.

In view of the above, the aim of this study is to investigate the characteristics of CrN coating formation on an E110 alloy substrate by magnetron sputtering and to analyze the influence of the working gas ratio (Ar/N_2) on the morphological, structural, physical, and mechanical characteristics of the coating.

2. Materials and methods

Samples of zirconium alloy E110 were used as substrates for coating. The surface of the substrates was pre-treated by mechanical grinding using abrasive paper with gradually decreasing grain size (from P400 to P2500). The chemical composition of the alloy is given in Table 2.

Table 2. Chemical composition of alloy E110 (mass%) according to GOST (State Standard), TS (Technical Specifications): 25278.10-82.

Zr	Be	Nb	Hf	Ni	Cr	Ti	Al	O	Pb
99.5	0.003	0.9–1.1	0.01	0.02	0.02	0.007	0.008	0.1	0.005

CrN coatings were applied by magnetron sputtering in a reactive atmosphere using a DC magnetron sputtering system. A metal plate made of pure chromium (99.95%) was used as the target. Deposition was carried out in an argon-nitrogen atmosphere with different Ar/N_2 gas ratios maintained by mass flow meters.

Before the sputtering process began, the substrate was heated to a temperature of 300 °C, after which a preliminary vacuum with a residual pressure of at least 5×10^{-3} Pa was created in the chamber. The working pressure during the sputtering process was 0.4–0.6 Pa. The distance between the target and the substrate was 40 mm. The substrate temperature was maintained at 300 °C. The negative potential voltage varied from –40 to –100 V to study its effect on coating formation.

Figure 1 shows a diagram of the installation, which includes the following main stages: after sealing the chamber, primary pumping is carried out using a fore-vacuum pump (3), then a turbomolecular pump (2) is switched on, ensuring that a residual pressure of about 10^{-3} to 10^{-6} Pa is achieved.

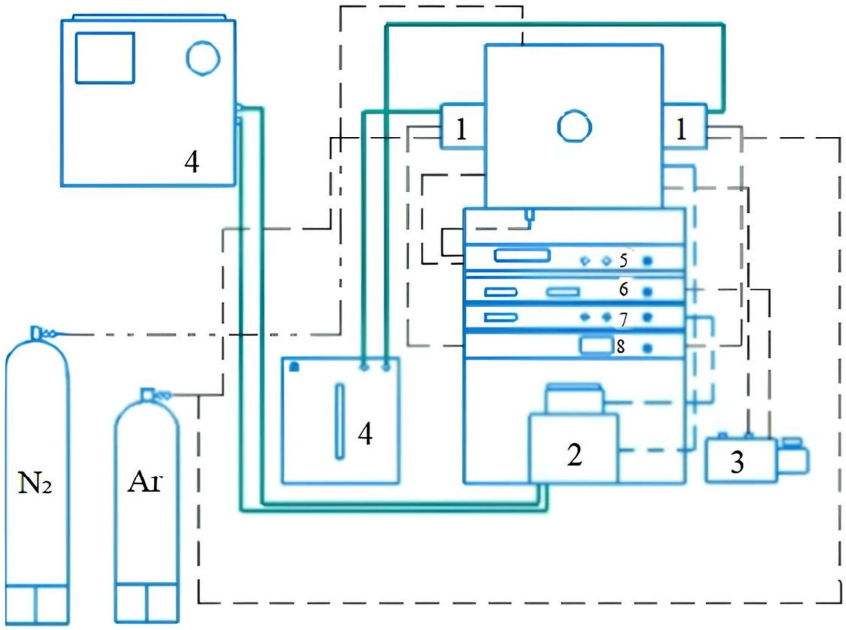

Figure 1. Schematic device of the installation for magnetron sputtering of CrN coating.

Gases are fed into the working chamber: Ar, which is necessary for plasma formation, and N_2, which participates in the formation of the nitride phase of the coating (CrN). The magnetron (1) is the main element of the installation and performs the spraying function. It creates a local magnetic field that helps to keep electrons near the target surface and increase the plasma density, which improves the efficiency of chromium atom sputtering. These atoms are deposited on a rotating substrate heated to a specified temperature, forming a coating. The bias unit (5) supplies a negative voltage (in a range from –40 to –100 V) to the substrate, which allows positively charged ions from the plasma to be attracted to its surface. This promotes ion cleaning and improves coating adhesion. The turbomolecular pump control unit (7) controls its activation, operation, and pressure stability in the chamber. The cooling system and control units (4 and 8) ensure the thermal stability of the magnetron and substrate and control the power supply, gases, deflection potential voltage, and other process parameters. Vacuum level and working pressure are monitored using appropriate sensors and a vacuum gauge (6). After spraying is complete, the gas supply is turned off, and the substrate cools down.

CrN coatings were applied under varying gas supply and power modes. The main technological parameters are presented in Table 3.

Table 3. CrN coating deposition modes using magnetron sputtering.

Samples/code example	Ar (sccm)	N_2 (sccm)	Power (W)	Deposition time (min)
Sample A1	90	30	200	60
Sample A2	85	35	200	120
Sample A3	80	40	200	180

The surface morphology and microstructure of the cross sections of the coatings were studied using a CIQTEK SEM3200 scanning electron microscope (SEM) (Hefei, Anhui, China) equipped with an XFlash Detector 730M-300 (Bruker) energy-dispersive X-ray microanalysis (EDS) system, which allowed additional determination of the elemental composition of the studied areas. An XRD-6000 X-ray diffractometer (Shimadzu, Japan) operating with Cu-Kα copper radiation (λ = 1.5406 Å) was used to analyze the phase composition of the coatings. X-ray structural analysis of the coatings was performed using the grazing incidence method (GI-XRD). Diffraction images were taken at an anode voltage of 40 kV and a current of 30 mA in the grazing incidence mode with an incidence angle of 1°. Diffractograms were recorded in the range of 2θ = 20–90°, with a scanning speed of 2°/min and a step of 0.05°. The coatings obtained with mechanical properties (Young's modulus, hardness) were studied using a NanoScan-4D Compact nanohardness tester (Federal State Budgetary Institution "TISNSM", Russia). Nanoindentation of coatings was performed using Oliver-Farr's method with a Berkovich indenter at a load of 100 mN (ASTM E2546-07). Surface roughness (Ra) was evaluated using an SSR300+ profilometer (Zhejiang, China). A CSEMMicroScratchTester (Neuchâtel, Switzerland) was used to study the adhesion characteristics of coatings using the "scratch" method. Scratch testing was performed at a maximum load of 5 N, with a normal loading rate of 4.99 N/min, an indenter travel speed of 9.63 mm/min, a scratch length of 10 mm, and a tip radius of curvature of 100 μm. Corrosion resistance was studied on a CS300M potentiostat–galvanostat. Coatings were tested with an open area of 1 cm^2 at room temperature (25 °C) in a 3.5 wt.% NaCl solution. The experiment used a three-electrode cell system, where a silver chloride electrode served as the reference electrode and a platinum electrode served as the auxiliary electrode. Before each polarization experiment, the sample was exposed to the electrolyte for 60 min of immersion until a stable open-circuit potential (OCP) was established. The corrosion potential and current density were obtained from the polarization curves using the Tafel extrapolation method for four samples. The potential was scanned in a range from –0.1 to 0.1 V relative to OCP at a scan rate of 0.5 mV/s. The tests were repeated three times, and the results were analyzed using CS Studio6 software (version 6.3). The chemical composition and distribution of elements across the depth of the coating were investigated using a GD Profiler 2 optical emission spectrometer (Horiba Scientific, France).

3. Results

Figure 2 presents the SEM analysis and EDS mapping results of the surface of the CrN coating deposited at an Ar/N_2 gas ratio of 90/30 sccm.

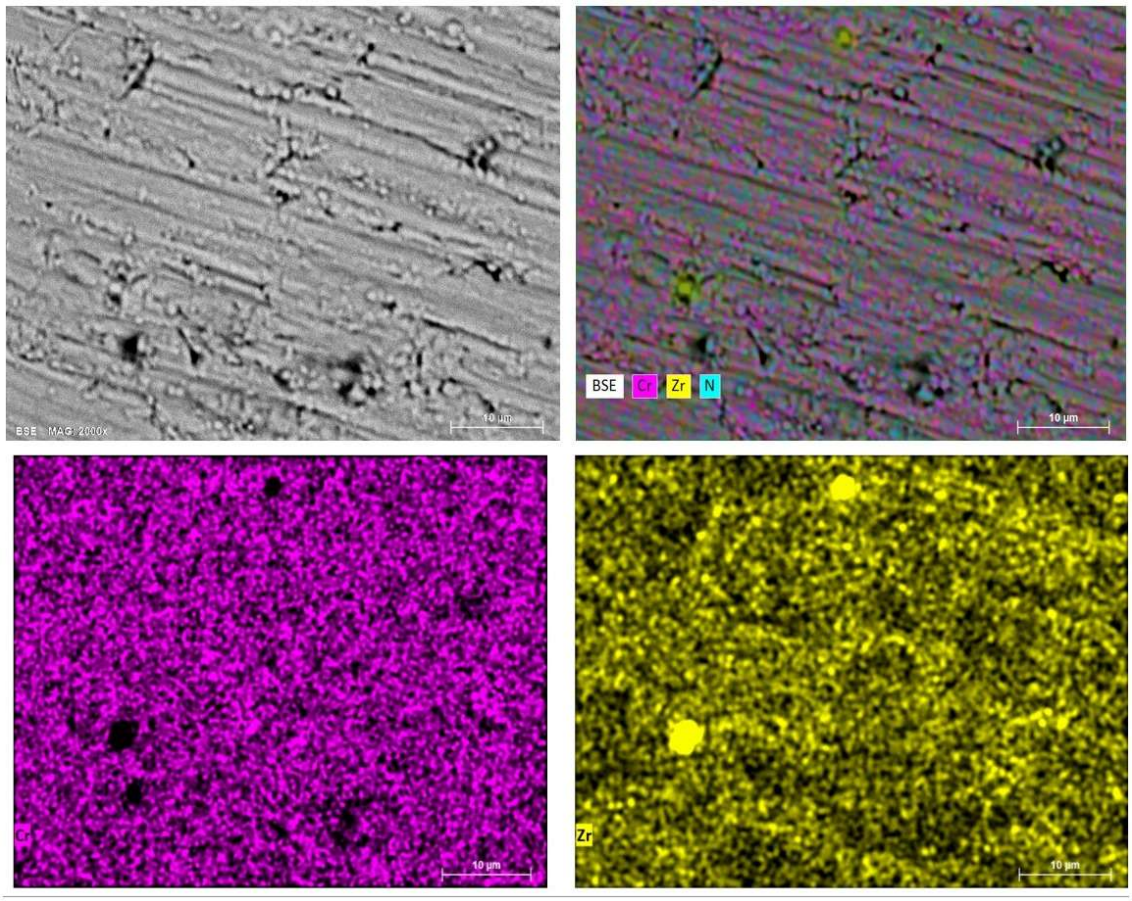

Map

Element	Atomic number	Line series	Net counts	Mass Concentration /%	Norm. mass concentration /%	Norm. atomic concentration /%	1σ uncertainty /mass%
N	7	K	8080	0.86	0.95	3.47	0.03
Cr	24	K	1346275	87.69	96.36	95.02	1.27
Zr	40	L	58179	2.45	2.69	1.51	0.06
			Sum	**91.01**	**100.00**	**100.00**	

Figure 2. Surface morphology and elemental analysis (EDS mapping) results for the CrN coating deposited at an Ar/N_2 gas ratio of 90/30 sccm.

The surface morphology of the CrN coating formed at an Ar/N_2 ratio of 90/30 sccm is characterized by a longitudinally oriented structure. According to the EDS data, the normalized mass concentration of nitrogen is 0.95%, while chromium predominates, reaching 96.36%.

Figure 3 shows the surface morphology of the CrN coating obtained at an Ar/N_2 gas ratio of 85/35 sccm.

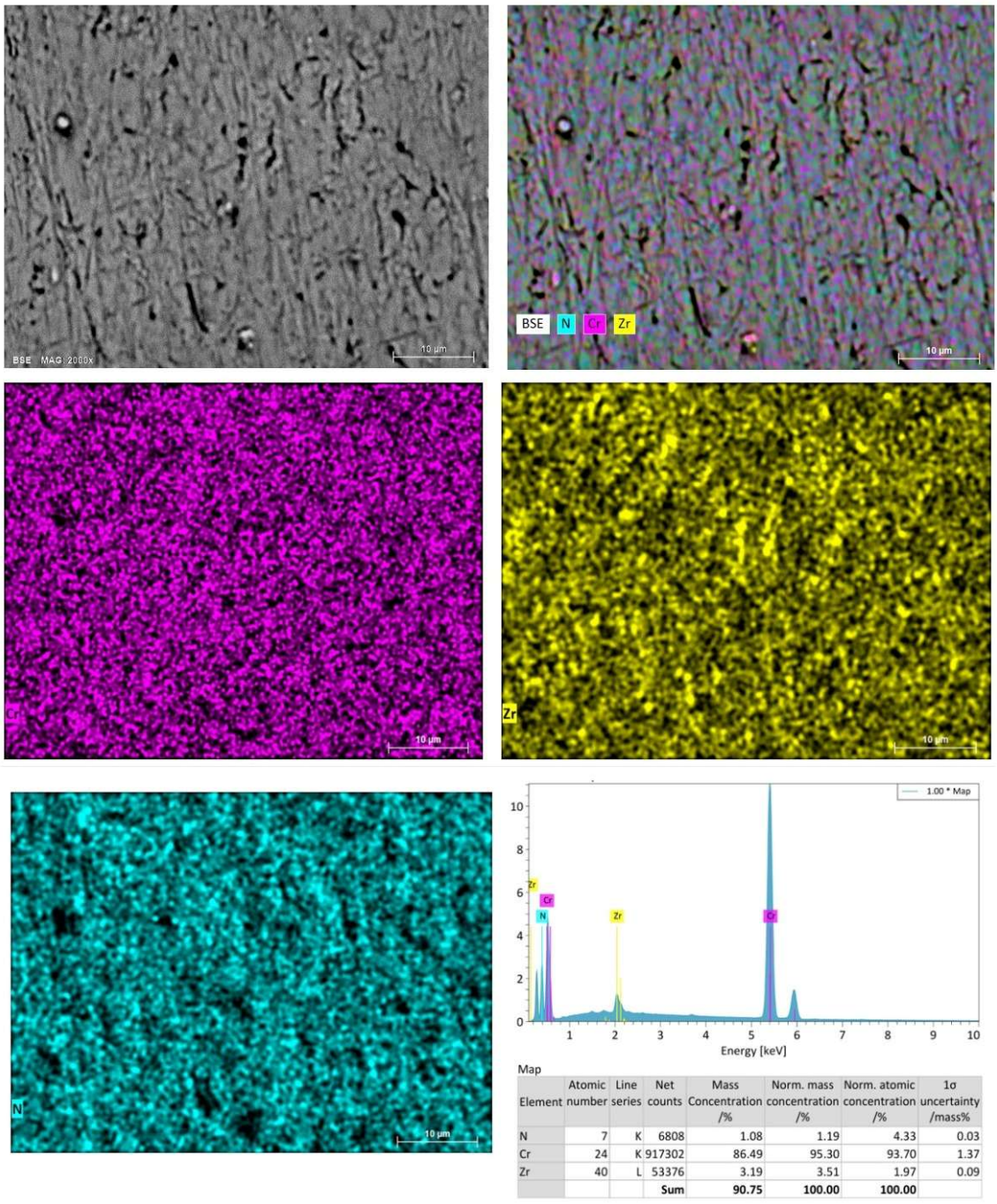

Map

Element	Atomic number	Line series	Net counts	Mass Concentration /%	Norm. mass concentration /%	Norm. atomic concentration /%	1σ uncertainty /mass%
N	7	K	6808	1.08	1.19	4.33	0.03
Cr	24	K	917302	86.49	95.30	93.70	1.37
Zr	40	L	53376	3.19	3.51	1.97	0.09
			Sum	**90.75**	**100.00**	**100.00**	

Figure 3. Surface morphology and elemental analysis (EDS mapping) results for the CrN coating deposited at an Ar/N_2 gas ratio of 85/35 sccm.

Under this deposition regime, the structure becomes finer-grained: the normalized mass concentration of nitrogen increases to 1.19%, while the chromium fraction decreases to 95.30%, indicating a more intensive formation of the nitride phase.

Figure 4 presents the surface morphology of the CrN coating formed at an Ar/N_2 gas ratio of 80/40 sccm.

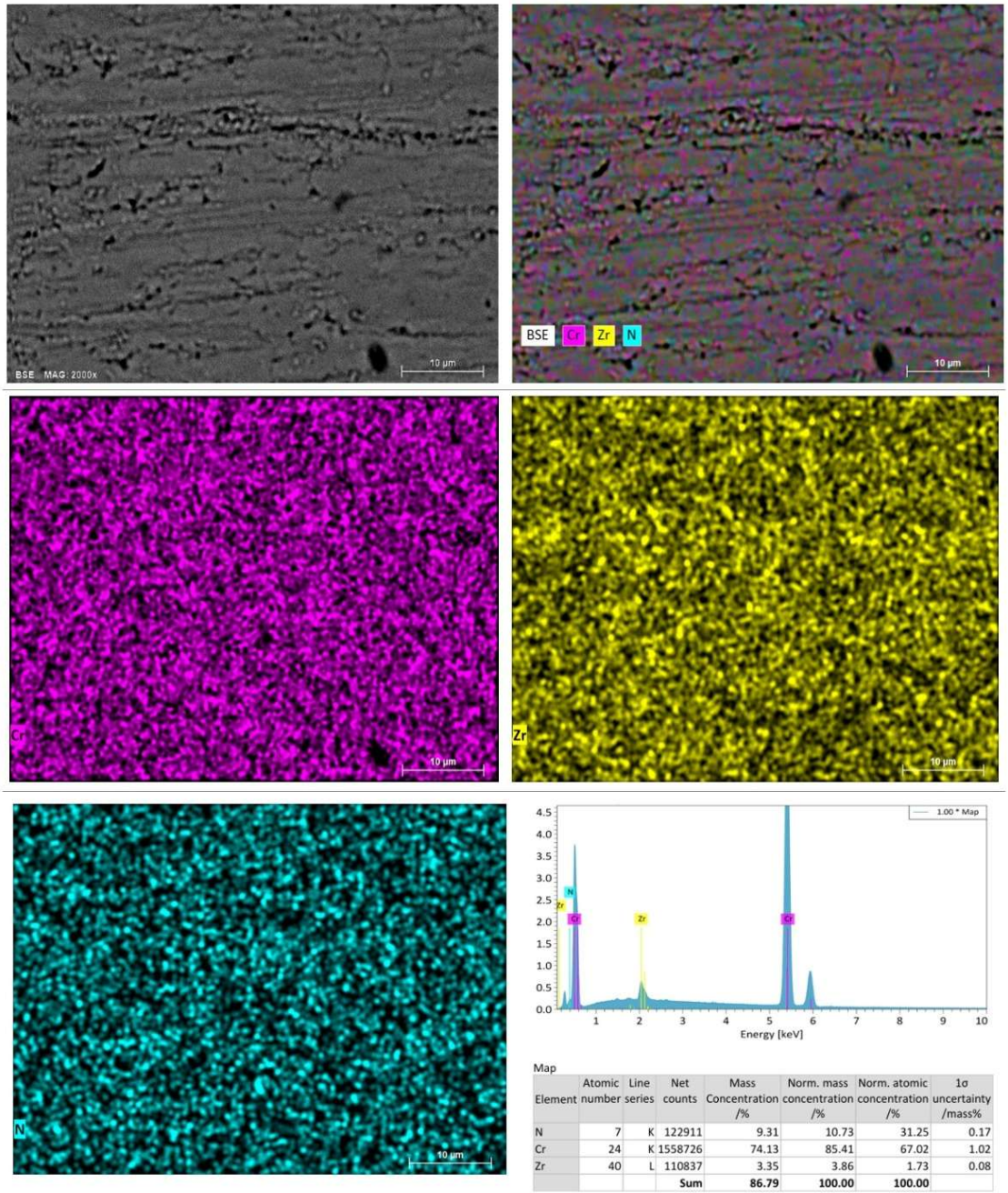

Map

Element	Atomic number	Line series	Net counts	Mass Concentration /%	Norm. mass concentration /%	Norm. atomic concentration /%	1σ uncertainty /mass%
N	7	K	122911	9.31	10.73	31.25	0.17
Cr	24	K	1558726	74.13	85.41	67.02	1.02
Zr	40	L	110837	3.35	3.86	1.73	0.08
			Sum	**86.79**	**100.00**	**100.00**	

Figure 4. Surface morphology and elemental analysis (EDS mapping) results for the CrN coating deposited at an Ar/N_2 gas ratio of 80/40 sccm.

Under this regime, the maximum degree of nitridation is achieved: the normalized mass concentration of nitrogen increases to 10.73%, while the chromium content decreases to 85.41%, corresponding to the most homogeneous and dense surface structure.

This trend indicates more intensive formation of nitride phases with increasing nitrogen partial pressure and is consistent with literature data on CrN_x coatings produced by reactive magnetron sputtering, where higher N_2 flow rates promote enhanced nitrogen incorporation and the transition to CrN-rich phases [57–60]. The Cr and N distribution maps for all samples show their uniform distribution across the surface, while the detected Zr signal (2.7%–3.9% normalized mass%) is attributed to the partial contribution of the substrate within the analyzed region.

Thus, the surface morphology of the CrN coatings (Figures 2–4), formed at different Ar/N_2 ratios, demonstrates a gradual densification of the structure and an increase in the degree of nitridation as the nitrogen fraction in the working gas mixture increases.

To clarify the distribution of elements across the coating thickness, an analysis was performed using optical emission glow discharge spectrometry. Figure 5 shows the profiles of element distribution across different depths.

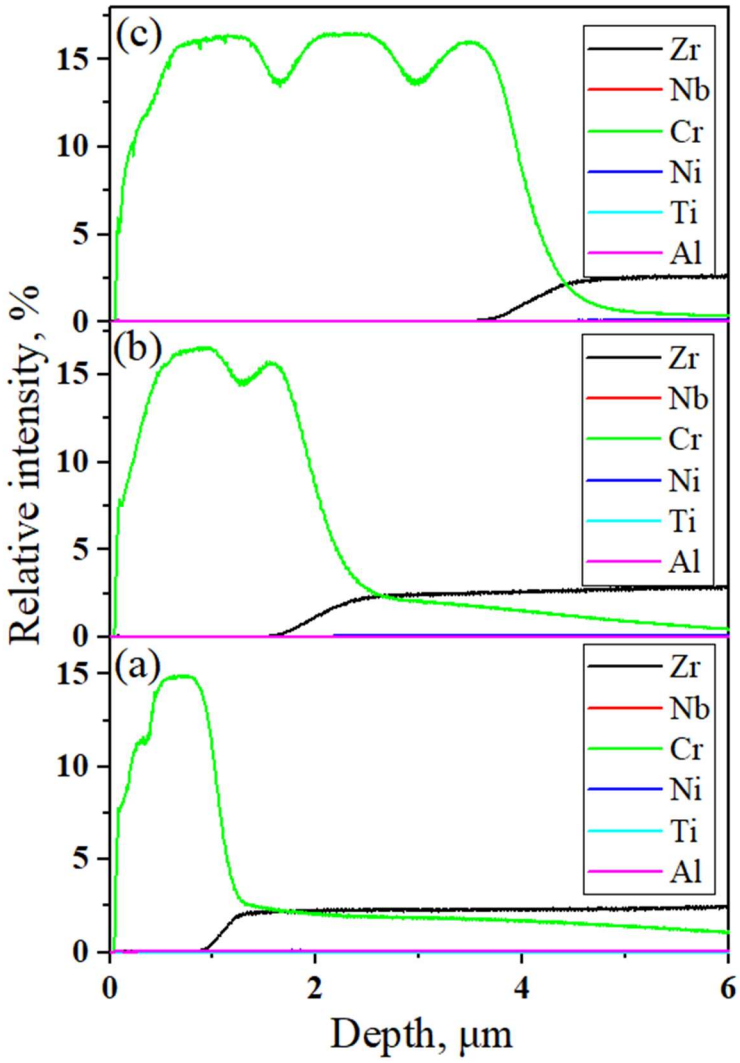

Figure 5. Profiles of the relative intensity of elements with depth, measured by optical emission glow discharge spectrometry for CrN coatings obtained at different Ar/N_2 gas ratios: (a) 90/30; (b) 85/35; (c) 80/40 sccm.

The glow discharge profiles (Figure 5) show a characteristic distribution of elements along the depth for all CrN coatings. In the near-surface zone (0–0.2 μm), the maximum relative intensity of the Cr line is recorded at about 10%–12%, while the contribution of the substrate elements (Zr, Nb) is practically zero. As the depth increases, the Cr intensity remains stable at ≈8%–10% until the coating boundary is reached. For the 90/30 sccm sample, the decrease in Cr intensity begins at a depth of ~1.6 μm, where a sharp increase in Zr intensity is simultaneously recorded, reflecting the transition to the substrate. For the 85/35 sccm mode, the length of the section with high Cr intensity increases slightly

and is ~1.7 μm, while the transition zone remains narrow (~0.2–0.3 μm). The maximum thickness of the nitride layer is observed at 80/40 sccm, where high Cr intensity values are maintained to a depth of ~2.0 μm, after which the Zr intensity increases, indicating the coating/substrate boundary. Ni, Ti, and Al signals remain at ≤1% throughout the depth. There is no noticeable oxygen intensity in any of the samples, confirming the absence of oxide phases in the coating structure.

Figure 6 shows cross sections of CrN coatings obtained at different working gas flows.

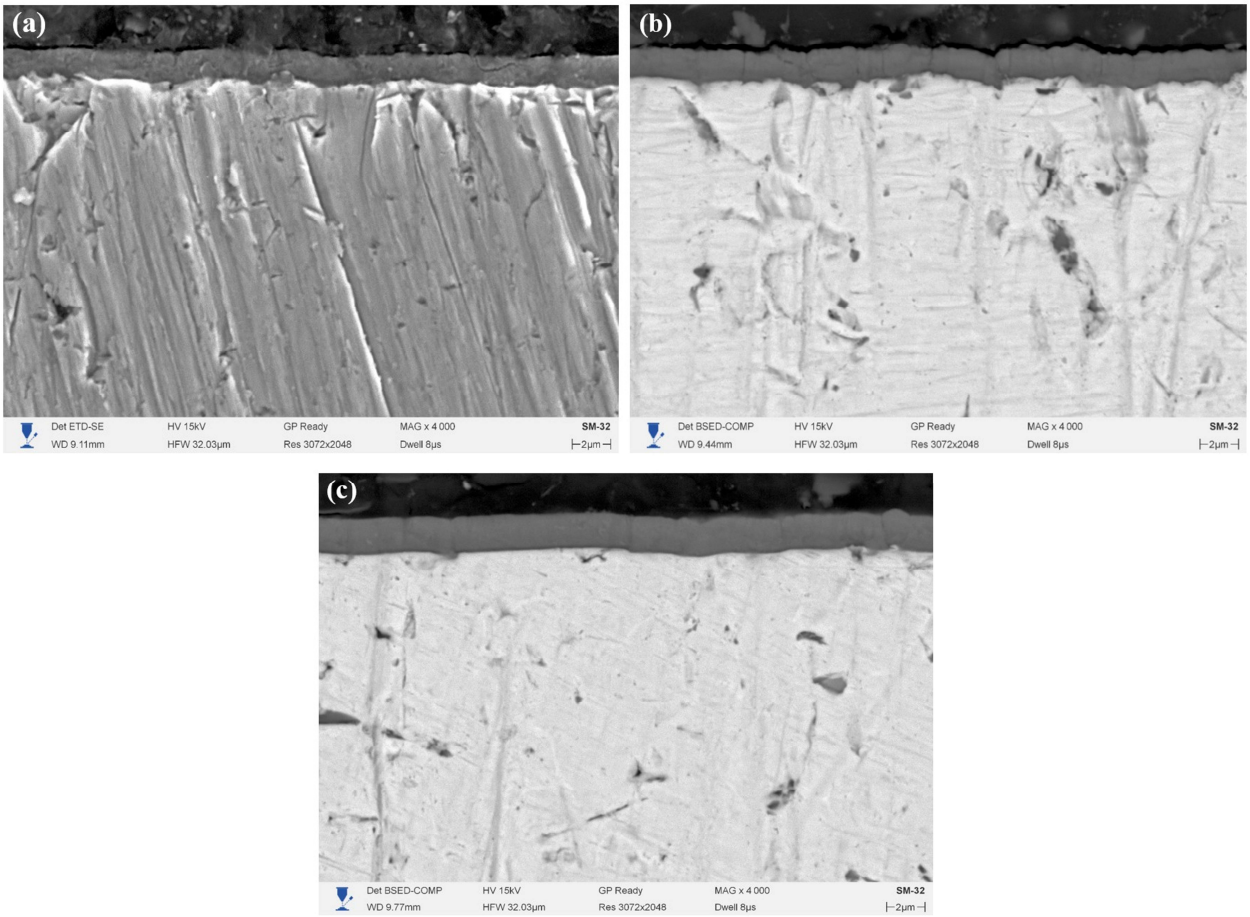

Figure 6. Cross sections of CrN coatings obtained by reactive magnetron sputtering at different Ar/N_2 gas ratios: (a) 90/30 sccm; (b) 85/35 sccm; (c) 80/40 sccm.

In all three modes, a typical columnar structure, oriented perpendicular to the substrate surface, was formed. The average film thickness values for each deposition mode are 1.62 ± 0.02 μm at a gas flow rate of Ar/N_2 = 90/30, 1.68 ± 0.08 μm at 85/35, and 1.96 ± 0.30 μm at 80/40. The slight increase in thickness with increasing N_2 flow rate reflects an increase in the rate of CrN nitride phase formation due to a higher degree of nitrogen saturation of the plasma and a decrease in the backsputtering of the already formed layer.

Figure 7 presents the elemental distribution results in the cross-section of the CrN coating obtained at an Ar/N_2 gas ratio of 90/30 sccm.

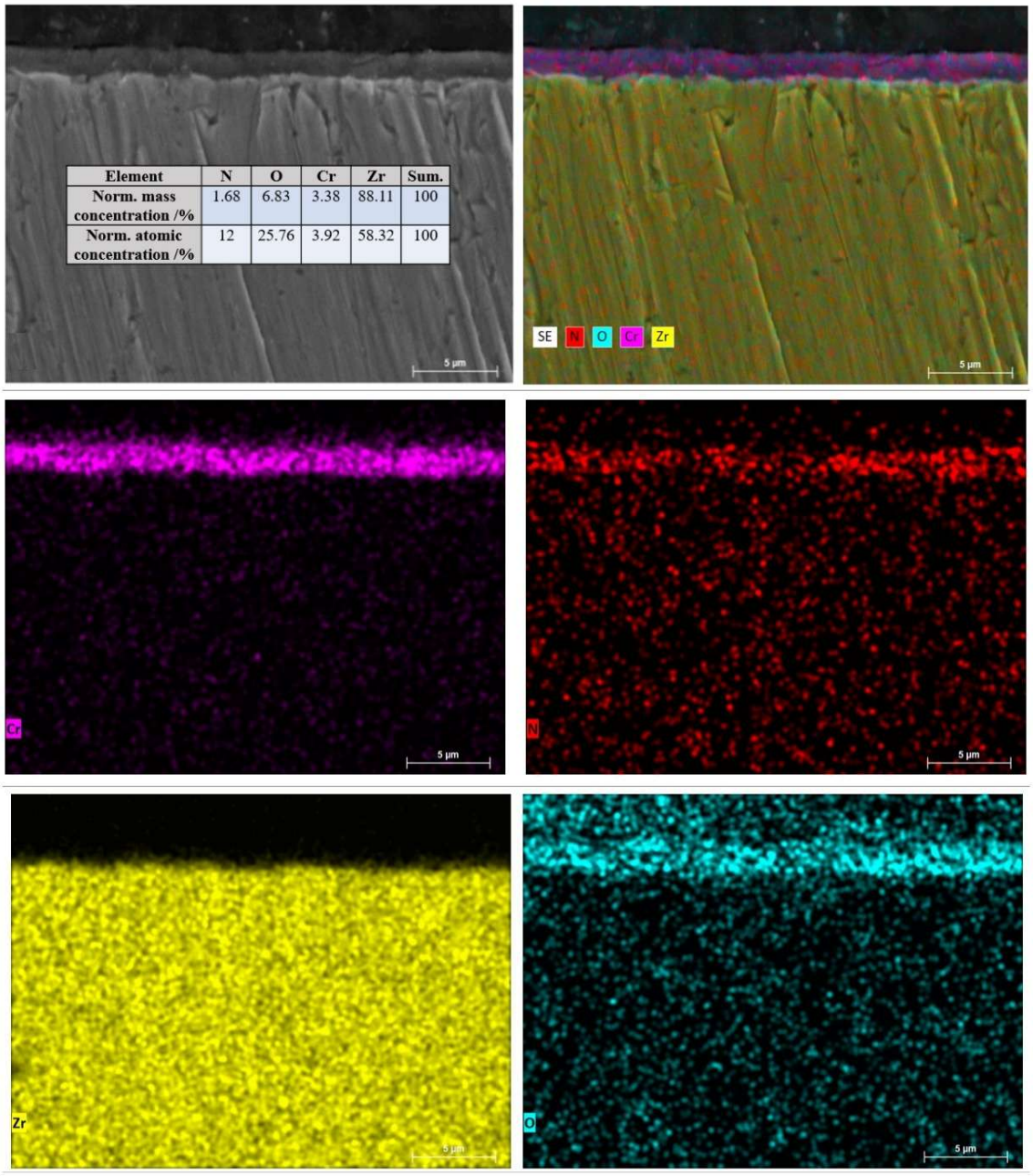

Figure 7. Elemental distribution maps in the cross-section of the CrN coating deposited at an Ar/N_2 ratio of 90/30 sccm.

EDS mapping shows that the CrN layer exhibits a stable and uniform distribution of Cr and N throughout the entire coating thickness. No signs of substrate element diffusion into the coating region were detected, indicating the formation of a dense and homogeneous nitride layer.

Further cross-sectional analysis was performed for the CrN coating obtained at an Ar/N_2 gas ratio of 85/35 sccm, as presented in Figure 8.

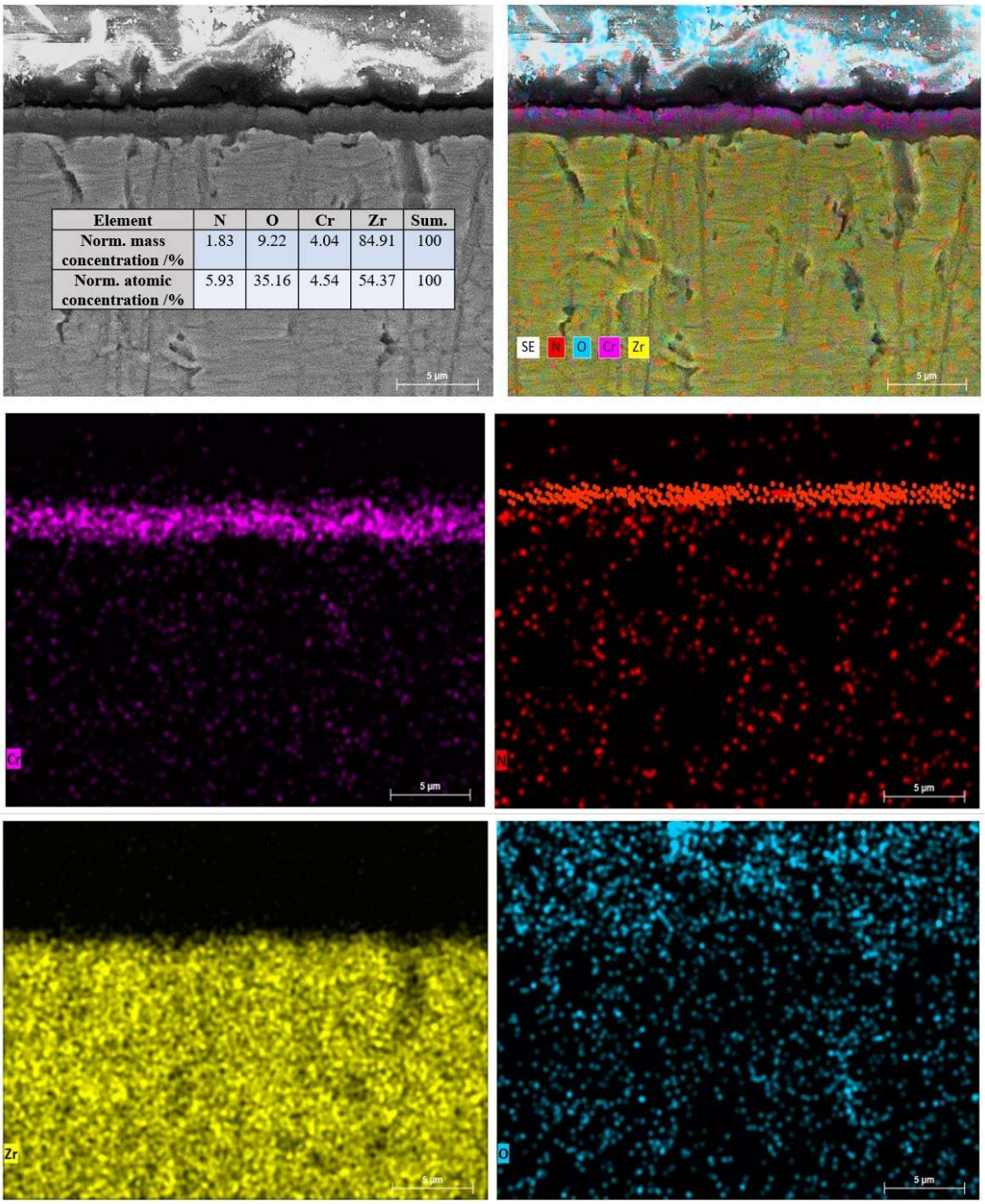

Figure 8. Elemental distribution maps in the cross-section of the CrN coating deposited at an Ar/N_2 ratio of 85/35 sccm.

EDS mapping reveals a pronounced enrichment of the surface layer with chromium and nitrogen, which is characteristic of nitride coating formation. At the same time, the Zr signal is detected exclusively in the substrate region, indicating a well-defined interface and the absence of diffusion mixing.

With an increase in the N_2 flow rate, an increase in the intensities of the Cr and N signals is observed, indicating a more complete nitridation of the film. This trend is clearly demonstrated in the results presented in Figure 9.

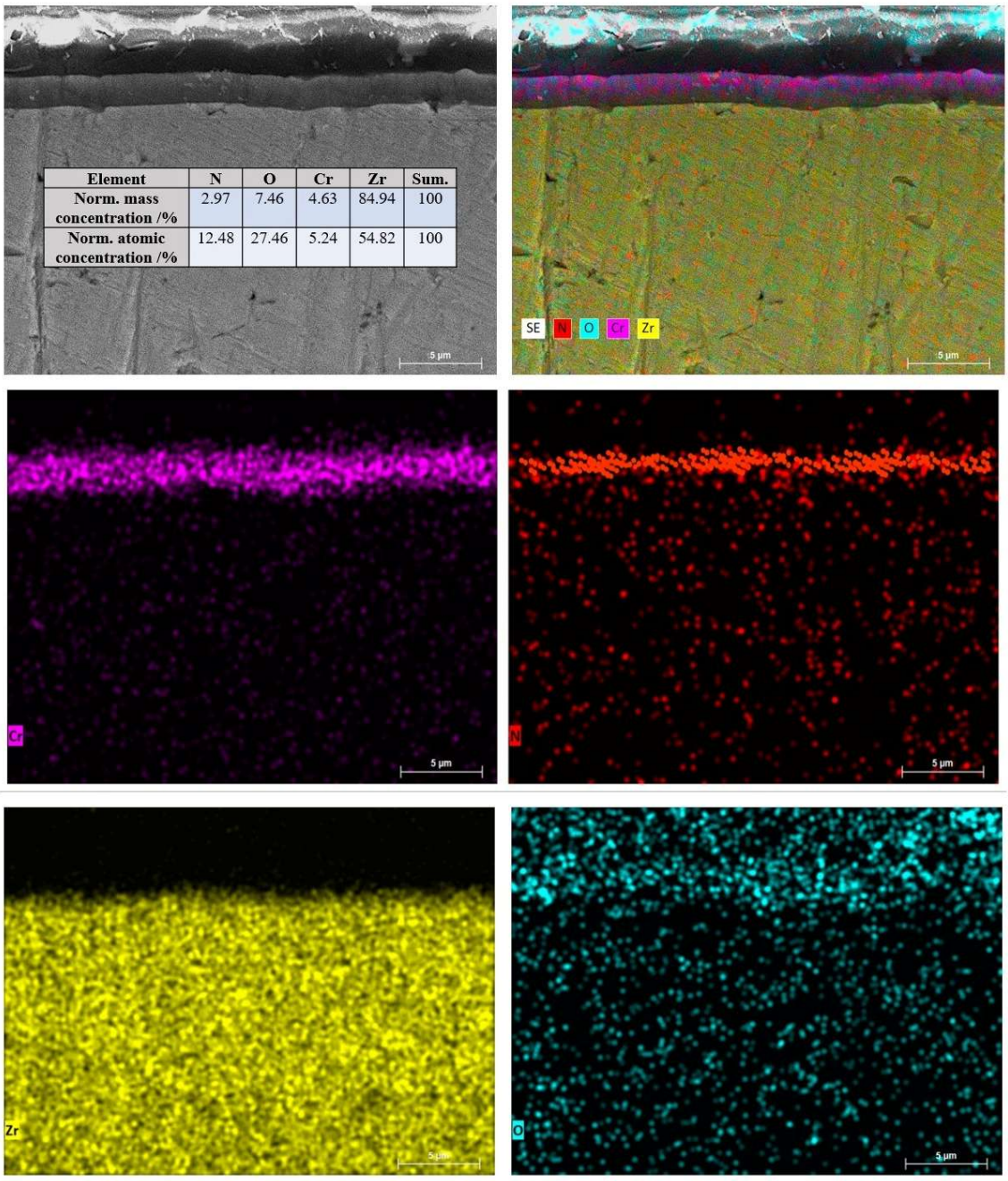

Figure 9. Elemental distribution maps in the cross-section of the CrN coating deposited at an Ar/N_2 ratio of 80/40 sccm.

The appearance of oxygen in the EDS spectra (Figures 7–9) is associated with the surface adsorption of oxygen-containing compounds and the limited analysis depth, in which the electron beam partially interacts with regions outside the coating. This is a typical feature of thin nitride films and does not indicate the presence of an oxide phase within the CrN layer [61,62].

Figure 10 shows the linear profiles of Cr, N, Zr, and O distribution through the thickness of CrN coatings obtained at Ar/N_2 ratios of 90/30, 85/35, and 80/40 sccm.

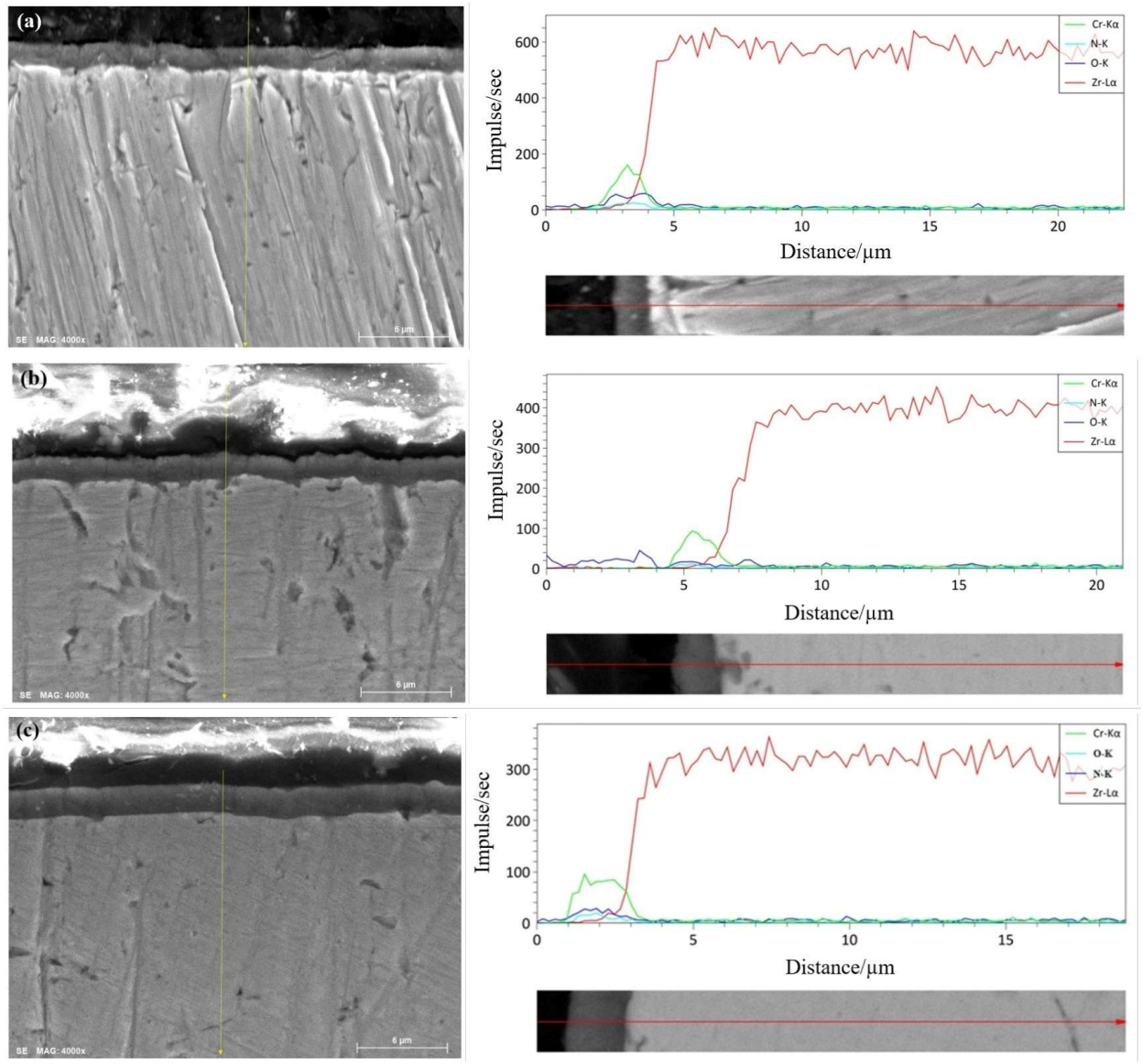

Figure 10. Results of linear EDS analysis of cross sections of coatings obtained by magnetron sputtering at different Ar/N_2 working gas ratios: (a) 90/30 sccm; (b) 85/35 sccm; (c) 80/40 sccm.

In all samples, the coating area is characterized by stable Cr-Kα and N-K signals, indicating a uniform composition of the CrN layer throughout its thickness. The Zr-Lα signal is absent inside the coating and increases sharply only at the boundary with the substrate, simultaneously with the drop of Cr and N to zero values, which confirms the presence of a clear interface boundary without signs of mutual diffusion. As the N_2 content increases, the length of the coating section on the profile increases, and the Cr and N levels become more even, which corresponds to an increase in film thickness and uniformity. The weak O-K signal does not show a structural distribution across the thickness and is not related to the coating composition. The profiles confirm the formation of a continuous CrN layer with a sharp substrate-coating boundary and improved uniformity with an increase in the nitrogen content in the working gas.

Furthermore, to obtain data specifically on the phase composition of the coatings, X-ray structural analysis was performed using the grazing incidence method (GI-XRD). The use of grazing beam geometry minimized the contribution of the substrate and allowed the registration of diffraction maxima formed by the CrN layer.

Figure 11 shows GI-XRD diffractograms of CrN coatings deposited at Ar/N_2 ratios of 90/30, 85/35, and 80/40 sccm.

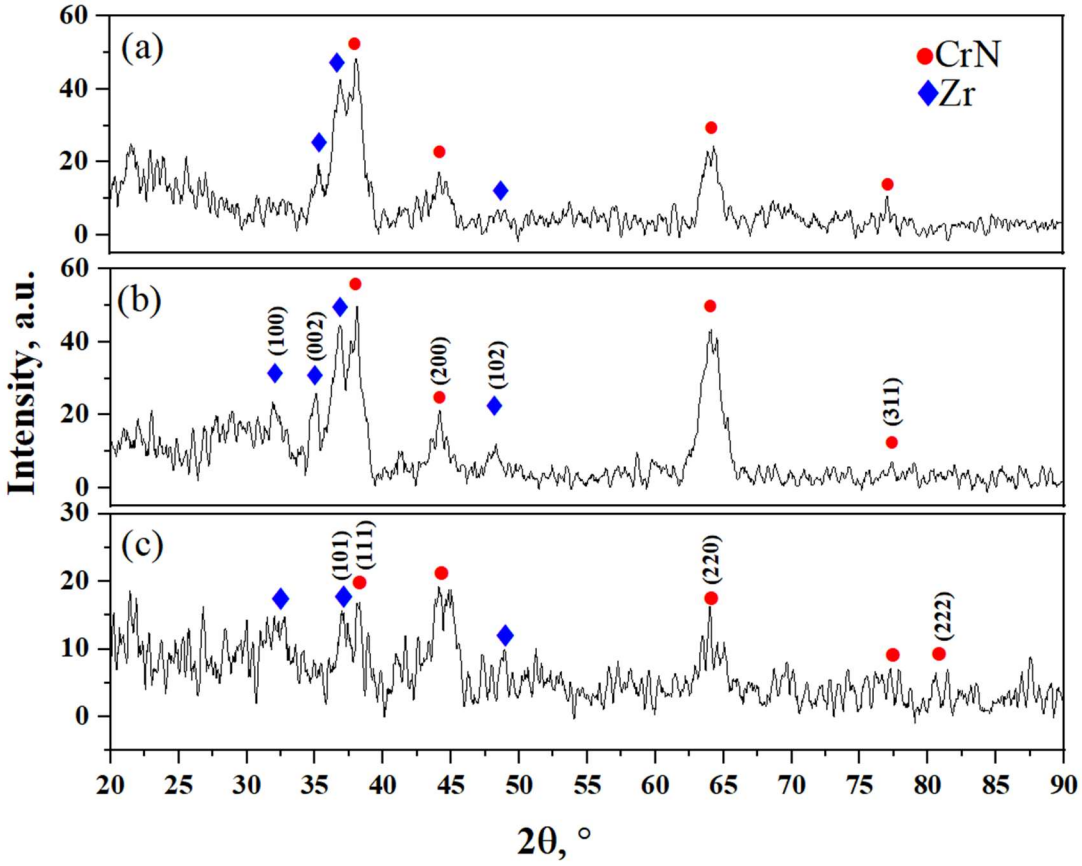

Figure 11. GI-XRD X-ray diffraction patterns of CrN coatings obtained by magnetron sputtering at different Ar/N_2 working gas ratios: (a) 90/30 sccm; (b) 85/35 sccm; (c) 80/40 sccm.

In all three cases, the diffraction patterns clearly show the peaks of the Zr substrate together with the reflections of the cubic phase of CrN. With an increase in nitrogen content, there is an increase in the intensity of the main CrN peaks: (111), (200), (220), (311), and (222). At the same time, the intensity of the Zr diffraction maxima decreases, which is associated with an increase in the contribution of the coating to the total X-ray signal. In the studied range of $2\theta = 20–90°$, there are no peaks corresponding to the oxide phases Cr_2O_3 and ZrO_2, and no such reflections were detected within the sensitivity of the method. Reference data from the ICDD PDF-2 database was used to identify the phases. Table 4 contains the CrN and Zr cards used to decipher the diffractograms.

Table 4. Data from the ICDD PDF-2 database.

Phase	Crystal lattice	Card index	Space group
CrN	Cubic	01-076-2494	Fm-3m
Zr	Hexagonal	00-001-1147	P63/mmc

As the partial pressure of nitrogen in the working gas increases (Ar/N_2: 90/30→85/35→80/40 sccm), the arithmetic mean roughness of the coating surface decreases monotonically: Ra = 0.152 ± 0.007, 0.150 ± 0.006, and 0.114 ± 0.006 μm, respectively. The decrease in Ra is associated with an increase in the degree of nitridation and ion-assisted compaction of the layer, which leads to the closure of intercolumnar voids, enlargement of crystallites, and a decrease in microdeformations, all of which reflect the relaxation of internal stresses and smoothing of the surface micro-relief.

In contrast, the nanohardness of CrN coatings increases monotonically. Figure 12 shows the nanohardness and Young's modulus values for these coatings as a function of gas flow rate, reflecting the influence of partial nitrogen pressure on their elastic-plastic characteristics.

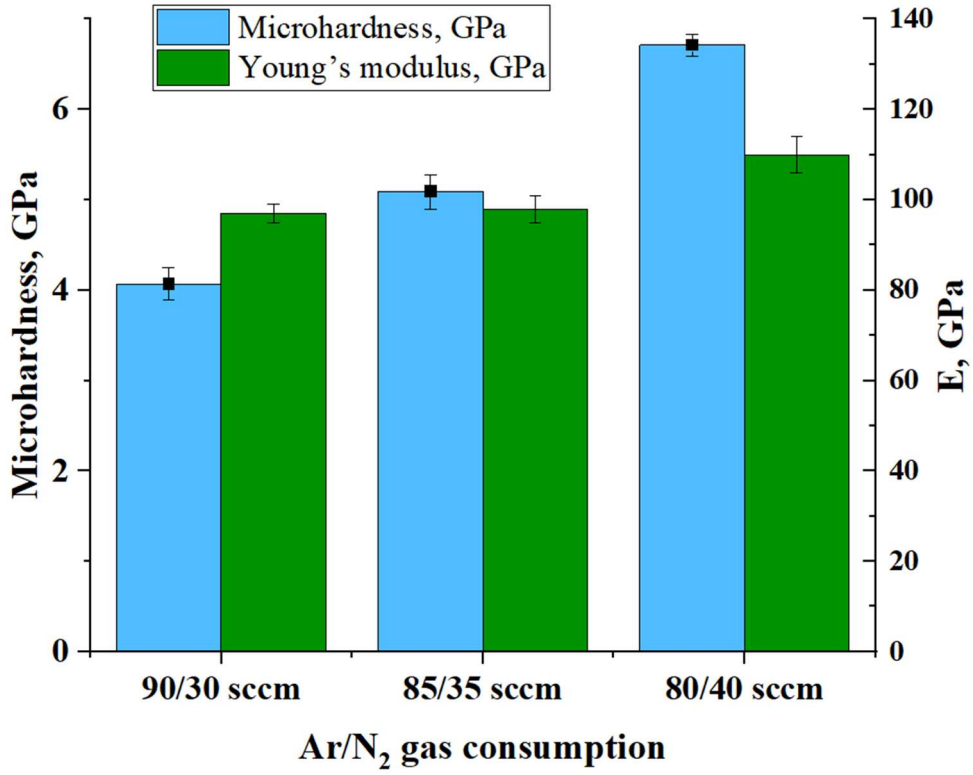

Figure 12. Nanohardness and Young's modulus of single-layer CrN coatings obtained at different Ar/N_2 gas flow ratios.

As can be seen from the data presented, increasing the nitrogen content in the gas mixture from 90/30 to 80/40 sccm leads to a sequential increase in both the nanohardness and Young's modulus of single-layer CrN coatings. At a flow rate of 90/30 sccm, the hardness and modulus values are approximately 4.1 ± 0.18 and 97 ± 2 GPa, respectively, which corresponds to a less dense and partially non-stoichiometric coating structure. The transition to the 85/35 sccm mode is accompanied by an

increase in hardness to ≈5.09 ± 0.19 GPa with a Young's modulus of about 98 ± 3 GPa, which reflects an improvement in the degree of nitridation. The maximum values (≈6.71 ± 0.12 and ≈110 ± 4 GPa) are observed at the 80/40 sccm mode, which is associated with the formation of a denser, stoichiometric CrN phase and a decrease in the defectiveness of the columnar structure.

Nevertheless, according to nanoindentation data, coatings exhibit relatively low hardness, which is due to a combination of structural and technological factors. First, coatings deposited at low nitrogen content form a columnar and partially loose morphology with pronounced intercolumnar defects, which reduces their resistance to indentation. Second, reduced N_2 consumption leads to the formation of non-stoichiometric CrN_x, which is characterized by lower hardness compared to the stoichiometric cubic CrN phase. Third, the relatively small thickness of the films (~1.6–2.0 μm) enhances the effect of the soft E110 substrate, which also leads to a decrease in the measured nanohardness values [63,64]. With an increase in nitrogen flow rate, the coating structure becomes denser and more homogeneous, the number of intercolumnar defects decreases, and the degree of nitride formation increases, which is consistent with a monotonic increase in nanohardness from 4.1 to 6.7 GPa.

Next, the corrosion resistance of CrN coatings was evaluated by the potentiodynamic polarization method with an open electrode area of 1 cm^2 in a NaCl solution with a concentration of 3.5 wt.% at 25 °C. The samples under study were obtained by reactive magnetron sputtering at working gas ratios of Ar/N_2 = 90/30, 85/35, and 80/40 sccm. The potentiodynamic polarization curves of CrN coatings are shown in Figure 13.

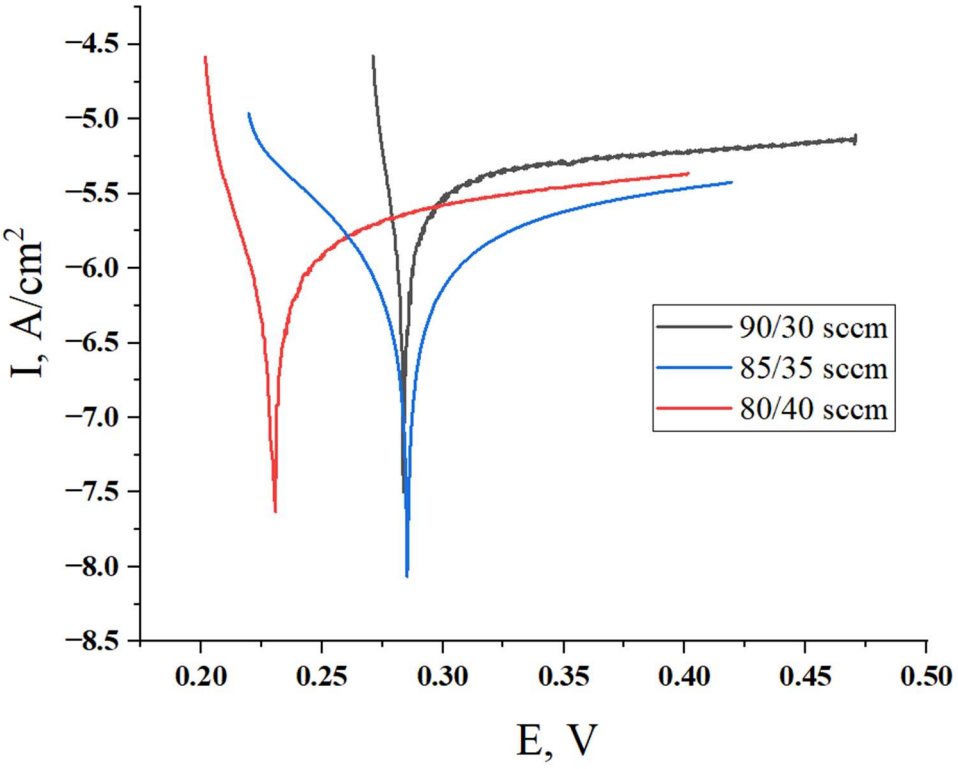

Figure 13. Potentiodynamic polarization curves of CrN coatings obtained by magnetron sputtering at different Ar/N_2 working gas ratios: (a) 90/30 sccm; (b) 85/35 sccm; and (c) 80/40 sccm.

As can be seen from the potentiodynamic curves (Figure 13), an increase in the nitrogen content in the gas mixture during CrN deposition leads to a sequential decrease in the corrosion current density and a shift in the corrosion potential to the negative side, which indicates an improvement in the corrosion resistance of the coating. The obtained electrochemical parameters (Table 5) demonstrate a decrease in Icorr from 3.82×10^{-6} A/cm^2 for the 90/30 mode to 1.73×10^{-6} A/cm^2 for the 80/40 mode and an almost 20-fold decrease in the corrosion rate, from 0.054 to 0.0024 mm/year.

Table 5. Corrosion test results.

Ar/N_2	90/30 sccm	85/35 sccm	80/40 sccm
E_{corr} (mV)	283	285	230
I_{corr} (A/cm^2)	3.82×10^{-6}	2.23×10^{-6}	1.73×10^{-6}
βc (mV)	27	111	50
βa (mV)	616	533	403
v_{corr} (mm/year)	0.054	0.031	0.0024

This trend is directly related to the evolution of the CrN structure as the partial pressure of nitrogen increases. A higher N_2 content promotes the formation of a dense, closer to stoichiometric CrN phase, characterized by a reduced number of defects and increased uniformity. Morphologically, this manifests itself in an increase in packing density and a decrease in the diameter of the columns forming the coating. A finer columnar structure reduces the number of intergranular channels through which electrolyte penetration usually occurs and reduces the likelihood of local galvanic microcouples [65–67].

An additional factor is the reduction in surface roughness at high nitrogen content. A smoother surface reduces the number of active anodic areas and slows down the rate of local Cr dissolution, which is confirmed by a decrease in the anodic slope βa (from 616 to 403 mV). On denser coatings, electrolyte access to defects is also impeded, leading to an increase in βc and a slowdown in cathodic reactions.

Thus, an increase in the nitrogen content in the plasma leads to an improvement in the density, morphology, and uniformity of CrN coatings, the formation of a higher-quality passive film and, as a result, a significant increase in their corrosion resistance.

4. Conclusions

1. It has been established that all CrN coatings obtained by reactive magnetron sputtering form a columnar structure with a clear boundary and uniform distribution of Cr and N throughout the thickness; there is no diffusion mixing with the substrate.

2. With an increase in N_2 content (from 90/30 to 80/40 sccm), a denser, more homogeneous, and closer to stoichiometric cubic phase of CrN is formed, which is confirmed by an increase in the intensity of the main diffraction reflections (111), (200), (220), (311), (222) and a decrease in the contribution of the Zr substrate.

3. The thickness of the coatings increases from 1.62 to 1.96 μm with an increase in N_2 in the gas mixture, which is associated with an increase in the degree of nitride formation and a decrease in the reverse spraying effect.

4. An increase in the nitrogen content leads to a decrease in surface roughness (Ra: 0.152 to 0.114 μm) and a simultaneous increase in nanohardness (4.1 to 6.7 GPa) and Young's modulus (97 to 110 GPa), which is explained by a decrease in defects and an increase in the density of the CrN layer.

5. Corrosion resistance increases significantly with increasing N_2 content: Icorr decreases by more than two times, and the corrosion rate decreases by almost 20 times (0.054 to 0.0024 mm/year), which is associated with a denser structure, lower porosity, and improved passive film formation.

Future work will focus on the development and investigation of multilayer Cr/CrN coatings (including 2-, 4-, and 6-layer structures) with the aim of increasing resistance to thermomechanical loads, improving barrier properties, and increasing operational reliability in conditions close to a nuclear environment.

Use of AI tools declaration

The authors declare they have not used Artificial Intelligence (AI) tools in the creation of this article.

Funding

This study was funded by the Committee of Science of the Ministry of Science and Higher Education of the Republic of Kazakhstan (grant No. AP19680681).

Author contributions

B.R. and N.M.: formal analysis, supervision, writing—review and editing; D.B. and E.T.: investigation, methodology; E.A. and M.D.: resources, data curation. All authors have read and agreed to the published version of the manuscript.

Conflict of interest

The authors declare no conflict of interest.

References

1. Ji PF, Li B, Liu SG, et al. (2020) Effect of laser surface re-melting on the microstructure and properties of Zr alloy. *Mater Lett* 264: 127352. https://doi.org/10.1016/j.matlet.2020.127352
2. Charit I (2018) Accident tolerant nuclear fuels and cladding materials. *JOM* 70: 173–175. https://doi.org/10.1007/s11837-017-2701-3
3. Duan Z, Yang H, Satoh Y, et al. (2017) Current status of materials development of nuclear fuel cladding tubes for light water reactors. *Nucl Eng Des* 316: 131–150. https://doi.org/10.1016/j.nucengdes.2017.02.031
4. Izmalkov IN, Loshmanov LP, Kostyukhina KAV (2013) Mechanical properties of E110 alloy at temperature range up to 1273 K. *Izv Vyssh Uchebn Zaved Yad Energ* 2: 71–79 (in Russian).
5. Perez-Feró E, Győri C, Matus L, et al. (2010) Experimental database of E110 claddings exposed to accident conditions. *J Nucl Mater* 397: 48–54. https://doi.org/10.1016/j.jnucmat.2009.12.005

6. Kim HG, Kim IH, Choi BK, et al. (2011) A study of the breakaway oxidation behavior of zirconium cladding materials. *J Nucl Mater* 418: 186–197. https://doi.org/10.1016/j.jnucmat.2011.06.039
7. Mazères B, Desgranges C, Toffolon-Masclet C, et al. (2016) Experimental study and numerical simulation of high temperature (1100–1250 °C) oxidation of prior-oxidized zirconium alloy. *Corros Sci* 103: 10–19. https://doi.org/10.1016/j.corsci.2015.10.018
8. Kim HG, Kim IH, Jung YI, et al. (2016) Development of surface modified Zr cladding by coating technology for ATF. Top Fuel, Boise, September 11–15, 2016.
9. Kim DH, Kim HC, Shin CH, et al. (2018) Development of deformation model for simulation of mechanical behaviors of coated-cladding. *J Nucl Sci Technol* 55: 1225–1234. https://doi.org/10.1080/00223131.2018.1486243
10. Bischoff J, Delafoy C, Vauglin C, et al. (2016) AREVA NP's enhanced accident-tolerant fuel developments: Focus on Cr-coated M5 cladding. *Nucl Eng Technol* 50: 223–228. https://doi.org/10.1016/j.net.2017.12.004
11. Li W, Wang Z, Shuai J, et al. (2019) A high oxidation resistance Ti_2AlC coating on Zirlo substrates for loss-of-coolant accident conditions. *Ceram Int* 45: 13912–13922. https://doi.org/10.1016/j.ceramint.2019.04.089
12. Chim YC, Ding XZ, Zeng XT, et al. (2009) Oxidation resistance of TiN, CrN, TiAlN and CrAlN coatings deposited by lateral rotating cathode arc. *Thin Solid Films* 517: 4845–4849. https://doi.org/10.1016/j.tsf.2009.03.038
13. Daub K, Van Nieuwenhove R, Nordin H (2015) Investigation of the impact of coatings on corrosion and hydrogen uptake of Zircaloy-4. *J Nucl Mater* 467: 260–270. https://doi.org/10.1016/j.jnucmat.2015.09.041
14. Park DJ, Kim HG, Park JY, et al. (2015) A study of the oxidation of FeCrAl alloy in pressurized water and high-temperature steam environment. *Corros Sci* 94: 459–465. https://doi.org/10.1016/j.corsci.2015.02.027
15. Koh HC, Hosemann P, Glaeser AM, et al. (2017) Compatibility studies on Mo–coating systems for nuclear fuel cladding applications. *J Nucl Mater* 496: 367–378. https://doi.org/10.1016/j.jnucmat.2017.09.034
16. Qi W, Yang K, Wang P, et al. (2022) High-temperature steam oxidation behavior of an FeCrAl alloy with controlled addition of Mo. *J Mater Sci* 57: 20909–20927. https://doi.org/10.1007/s10853-022-07920-3
17. Yeom H, Maier B, Johnson G, et al. (2019) High temperature oxidation and microstructural evolution of cold spray chromium coatings on Zircaloy-4 in steam environments. *J Nucl Mater* 526: 151737. https://doi.org/10.1016/j.jnucmat.2019.151737
18. Han X, Xue J, Peng S, et al. (2019) An interesting oxidation phenomenon of Cr coatings on Zry-4 substrates in high temperature steam environment. *Corros Sci* 156: 117–124. https://doi.org/10.1016/j.corsci.2019.05.017
19. Huntz AM (1995) Stresses in NiO, Cr_2O_3 and Al_2O_3 oxide scales. *Mater Sci Eng* 201: 211–228. https://doi.org/10.1016/0921-5093(94)09747-X
20. Chen QS, Liu CH, Zhang RQ, et al. (2020) Microstructure and high-temperature steam oxidation properties of thick Cr coatings prepared by magnetron sputtering for accident tolerant fuel claddings: The role of bias in the deposition process. *Corros Sci* 165: 108378. https://doi.org/10.1016/j.corsci.2019.108378

21. Blanco D, Viesca JL, Mallada MT, et al. (2016) Wettability and corrosion of [NTf2] anion-based ionic liquids on steel and PVD (TiN, CrN, ZrN) coatings. *Surf Coat Technol* 302: 13–21. https://doi.org/10.1016/j.surfcoat.2016.05.051
22. Chen L, Xu YX, Zhang LJ (2016) Influence of TiN and ZrN insertion layers on the microstructure, mechanical and thermal properties of Cr–Al–N coatings. *Surf Coat Technol* 285: 146–152. https://doi.org/10.1016/j.surfcoat.2015.11.033
23. Gilewicz A, Chmielewska P, Murzynski D, et al. (2016) Corrosion resistance of CrN and CrCN/CrN coatings deposited using cathodic arc evaporation in Ringer's and Hank's solutions. *Surf Coat Technol* 299: 7–14. https://doi.org/10.1016/j.surfcoat.2016.04.069
24. Lei Z, Liu Y, Ma F, et al. (2016) Oxidation resistance of TiAlN/ZrN multilayer coatings. *Vacuum* 127: 22–29. https://doi.org/10.1016/j.vacuum.2016.02.004
25. Zuo J, Xie Y, Zhang J, et al. (2015) TiN coated stainless steel bracket: Tribological, corrosion resistance, biocompatibility and mechanical performance. *Surf Coat Technol* 277: 227–233. https://doi.org/10.1016/j.surfcoat.2015.07.009
26. Meng C, Yang L, Wu Y, et al. (2019) Study of the oxidation behavior of CrN coating on Zr alloy in air. *J Nucl Mater* 515: 354–369. https://doi.org/10.1016/j.jnucmat.2019.01.006
27. Lin J, Zhang N, Sproul WD, et al. (2012) A comparison of the oxidation behavior of CrN films deposited using continuous dc, pulsed dc and modulated pulsed power magnetron sputtering. *Surf Coat Technol* 206: 3283–3290. https://doi.org/10.1016/j.surfcoat.2012.01.033
28. Qu Z, Shang G, Ma S, et al. (2022) Friction and wear properties of Cr-Nx coatings for nuclear fuel cladding. *Coatings* 12: 163. https://doi.org/10.3390/coatings12020163
29. Wongpanya P, Tunmee S, Euaruksakul C, et al. (2014) Corrosion behaviors and mechanical properties of CrN film. *Adv Mater Res* 853: 155–163. https://doi.org/10.4028/www.scientific.net/AMR.853.155
30. Adesina AY, Gasem ZM, Mohammed AS (2019) Comparative investigation and characterization of the scratch and wear resistance behavior of TiN, CrN, AlTiN and AlCrN cathodic arc PVD coatings. *Arab J Sci Eng* 44: 10355–10371. https://doi.org/ 10.1007/s13369-019-04038-8
31. Ali LA, Dikici B, Aslan N, et al. (2023) In-vitro corrosion and surface properties of PVD-coated β-type TNTZ alloys for potential usage as biomaterials: Investigating the hardness, adhesion, and antibacterial properties of TiN, ZrN, and CrN film. *Surf Coat Technol* 466: 129624. https://doi.org/10.1016/j.surfcoat.2023.129624
32. Fenker M, Balzer M, Kappl H (2014) Corrosion protection with hard coatings on steel: Past approaches and current research efforts. *Surf Coat Technol* 257: 182–205. https://doi.org/10.1016/j.surfcoat.2014.08.069
33. Warcholiński B, Gilewicz A, Kukliński Z, et al. (2008) Arc-evaporated CrN, CrN and CrCN coatings. *Vacuum* 83: 715–718. https://doi.org/10.1016/j.vacuum.2008.05.005
34. Warcholinski B, Gilewicz A (2013) Effect of substrate bias voltage on the properties of CrCN and CrN coatings deposited by cathodic arc evaporation. *Vacuum* 90: 145–150. https://doi.org/10.1016/j.vacuum.2012.04.039
35. Lin J, Sproul WD, Moore JJ, et al. (2011) High rate deposition of thick CrN and Cr_2N coatings using modulated pulse power (MPP) magnetron sputtering. *Surf Coat Technol* 205: 3226–3234. https://doi.org/10.1016/j.surfcoat.2010.11.039

36. Wang D, Hu M, Jiang D, et al. (2017) The improved corrosion resistance of sputtered CrN thin films with Cr-ion bombardment layer by layer. *Vacuum* 143: 329–335. https://doi.org/10.1016/j.vacuum.2017.06.040
37. Reinhold E, Faber J (2011) Large area electron beam physical vapor deposition (EB-PVD) and plasma activated electron beam (EB) evaporation—Status and prospects. *Surf Coat Technol* 206: 1653–1659. https://doi.org/10.1016/j.surfcoat.2011.09.022
38. Avelar-Batista JC, Spain E, Housden J, et al. (2005) Characterisation of pristine and recoated electron beam evaporation plasma-assisted physical vapour deposition Cr–N coatings on AISI M2 steel and WC–Co substrates. *Thin Solid Films* 491: 177–183. https://doi.org/10.1016/j.tsf.2005.06.029
39. Sabitzer C, Steinkellner C, Koller CM, et al. (2015) Diffusion behavior of C, Cr, and Fe in arc evaporated TiN- and CrN-based coatings and their influence on thermal stability and hardness. *Surf Coat Technol* 275: 185–192. https://doi.org/10.1016/j.surfcoat.2015.05.020
40. Buitkenov D, Rakhadilov B, Nabioldina A, et al. (2024) Investigation of structural phase, mechanical, and tribological characteristics of layer gradient heat-protective coatings obtained by the detonation spraying method. *Materials* 17: 5253. https://doi.org/10.3390/ma17215253
41. Rakhadilov BK, Kenesbekov AB, Sagdoldina ZB, et al. (2020) Tribological and corrosion characteristics of coatings based on chromium nitride deposited by the mechanochemical method. *J Phys Conf Ser* 1529: 042101. https://doi.org/10.1088/1742-6596/1529/4/042101
42. Lee JW, Tien SK, Kuo YC, et al. (2006) The mechanical properties evaluation of the CrN coatings deposited by the pulsed DC reactive magnetron sputtering. *Surf Coat Technol* 200: 3330–3335. https://doi.org/10.1016/j.surfcoat.2005.07.047
43. Flores M, Huerta L, Escamilla R, et al. (2007) Effect of substrate bias voltage on corrosion of TiN/Ti multilayers deposited by magnetron sputtering. *Appl Surf Sci* 253: 7192–7196. https://doi.org/10.1016/j.apsusc.2007.02.203
44. Kelly PJ, Arnell RD (2000) Magnetron sputtering: A review of recent developments and applications. *Vacuum* 56: 159–172. https://doi.org/10.1016/S0042-207X(99)00189-X
45. Prabakaran M, Suresh Kumar S, Ramyesh KR, et al. (2014) Characterization and optimization of CrN coatings on tool steels (6959). *Int J Mech Ind Technol* 2: 108–112.
46. Shan L, Wang Y, Li J, et al. (2014) Effect of N_2 flow rate on microstructure and mechanical properties of PVD CrN_x coatings for tribological application in seawater. *Surf Coat Technol* 242: 74–82. https://doi.org/10.1016/j.surfcoat.2014.01.021
47. Cheng Y, Zheng YF (2006) Effect of N_2/Ar gas flow ratio on the deposition of TiN/Ti coatings on NiTi shape memory alloy by PIIID. *Mater Lett* 60: 2243–2247. https://doi.org/10.1016/j.matlet.2005.12.147
48. Kehal A, Saoula N, Abaidia SEH, et al. (2021) Effect of Ar/N_2 flow ratio on the microstructure and mechanical properties of Ti-Cr-N coatings deposited by DC magnetron sputtering on AISI D2 tool steels. *Surf Coat Technol* 421: 127444. https://doi.org/10.1016/j.surfcoat.2021.127444
49. Kong Q, Ji L, Li H, et al. (2011) Composition, microstructure, and properties of CrN_x films deposited using medium frequency magnetron sputtering. *Appl Surf Sci* 257: 2269–2274. https://doi.org/10.1016/j.apsusc.2010.09.086
50. Zhang H, Duo SW, Xu XM, et al. (2014) Effect of N_2 flow rate on structure and mechanical properties of CRN coatings prepared by closed field unbalanced magnetron sputtering. *Key Eng Mater* 591: 95–98. https://doi.org/10.4028/www.scientific.net/KEM.591.95

51. Ahmad R, Ali N, Khan IA, et al. (2013) Effect of power and nitrogen content on the deposition of CrN films by using pulsed DC magnetron sputtering plasma. *Plasma Sci Technol* 15: 666. https://doi.org/10.1088/1009-0630/15/7/12
52. Zhang H, Shang J, Luo CG, et al. (2016) Influence of nitrogen content on properties of CrN coatings deposited by single target magnetron sputtering. *Key Eng Mater* 680: 502–506. https://doi.org/10.4028/www.scientific.net/KEM.680.502
53. Zhang GA, Yan PX, Wang P, et al. (2007) Influence of nitrogen content on the structural, electrical and mechanical properties of CrN_x thin films. *Mater Sci Eng* 460–461: 301–305. https://doi.org/10.1016/j.msea.2007.01.149
54. Subramanian B, Prabakaran K, Jayachandran M (2012) Influence of nitrogen flow rates on materials properties of CrN_x films grown by reactive magnetron sputtering. *Bull Mater Sci* 35: 505–511. https://doi.org/10.1007/s12034-012-0344-0
55. Shah HN, Jayaganthan R, Kaur D, et al. (2010) Influence of sputtering parameters and nitrogen on the microstructure of chromium nitride thin films deposited on steel substrate by direct-current reactive magnetron sputtering. *Thin Solid Films* 518: 5762–5768. https://doi.org/10.1016/j.tsf.2010.05.095
56. He Y, Gao K, Yang H, et al. (2021) Nitrogen effects on structure, mechanical and thermal fracture properties of CrN films. *Ceram Int* 47: 30729–30740. https://doi.org/10.1016/j.ceramint.2021.07.252
57. Forniés E, Galindo RE, Sánchez O, et al. (2006) Growth of CrN_x films by DC reactive magnetron sputtering at constant N_2/Ar gas flow. *Surf Coat Technol* 200: 6047–6053. https://doi.org/10.1016/j.surfcoat.2005.09.020
58. Garzon-Fontecha A, Castillo HA, Restrepo-Parra E, et al. (2018) The role of the nitrogen flow rate on the transport properties of CrN thin films produced by DC magnetron sputtering. *Surf Coat Technol* 334: 98–104. https://doi.org/10.1016/j.surfcoat.2017.11.009
59. Liu YC, Hsiao SN, Chen YH, et al. (2023) High-power impulse magnetron sputter-deposited chromium-based coatings for corrosion protection. *Coatings* 13: 2101. https://doi.org/10.3390/coatings13122101
60. Elo R, Jacobson S, Kubart T (2020) Tailoring residual stresses in CrN_x films on alumina and silicon deposited by high-power impulse magnetron sputtering. *Surf Coat Technol* 397: 125990. https://doi.org/10.1016/j.surfcoat.2020.125990
61. Li Z, Liu C, Chen Q, et al. (2021) Microstructure, high-temperature corrosion and steam oxidation properties of Cr/CrN multilayer coatings prepared by magnetron sputtering. *Corros Sci* 191: 109755. https://doi.org/10.1016/j.corsci.2021.109755
62. Musil J (2000) Hard and superhard nanocomposite coatings. *Surf Coat Technol* 125: 322–330. https://doi.org/10.1016/S0257-8972(99)00586-1
63. Nualkham I, Sakdanuphab R, Sakulkalavek A (2017) Improvement of structural, morphological and mechanical properties of CrN_x sputtered thin films by vacuum annealing process. *Key Eng Mater* 751: 113–118. https://doi.org/10.4028/www.scientific.net/KEM.751.113
64. Mayrhofer PH, Tischler G, Mitterer C (2001) Microstructure and mechanical/thermal properties of Cr–N coatings deposited by reactive unbalanced magnetron sputtering. *Surf Coat Technol* 142: 78–84. https://doi.org/10.1016/S0257-8972(01)01090-8
65. Wan Z, Zhang TF, Ding JC, et al. (2017) Enhanced corrosion resistance of PVD-CrN coatings by ALD sealing layers. *Nanoscale Res Lett* 12: 248. https://doi.org/10.1186/s11671-017-2020-1

66. Ahn SH, Choi YS, Kim JG, et al. (2002) A study on corrosion resistance characteristics of PVD Cr-N coated steels by electrochemical method. *Surf Coat Technol* 150: 319–326. https://doi.org/10.1016/S0257-8972(01)01529-8
67. Han Z, Tian J, Lai Q, et al. (2003) Effect of N_2 partial pressure on the microstructure and mechanical properties of magnetron sputtered CrN_x films. *Surf Coat Technol* 162: 189–193. https://doi.org/10.1016/S0257-8972(02)00667-9

AIMS Press